Surface Reconstruction-Driven WCuNiMo Alloy for Efficient Ammonia Oxidation and Hydrogen Evolution

Fozia Sultana[a,+], Jichao Shi [b,+], Renkun Li[a], Kexin Sun[a], Wang Qiurong[a], Ting Xiao[a], Xiaoqing Yan[b], Tong Wei[a], Renhong Li[a,*]

Physical Characterization of Materials

The phase composition and crystal structure of the samples were analyzed using an X-ray diffraction (XRD) instrument (model DX-2700, Dandong Fangyuan Instrument Co., Ltd.) with a scanning step size of 0.02°, a scan range of 20-80°, and a tube voltage range of 10-60 kV. The chemical composition and valence states of elements in the samples were determined using an X-ray photoelectron spectroscopy (XPS) instrument (model K-Alpha, Thermo Fisher Scientific, USA). The binding energy values were calibrated using the C 1s peak at 284.8 eV as the reference. The surface morphology of the samples was observed using a field emission scanning electron microscope (FE-SEM, model Sigma 300, ZEISS, Germany) at magnifications ranging from 200 nm to 1 μm. An energy dispersive spectrometer (EDS) was used in conjunction with SEM to analyze the elemental distribution. A transmission electron microscope (TEM, model Tecnai F30, FEI, USA) with an accelerating voltage of 300 kV was employed to further investigate the lattice structure of the samples at the nanoscale. The bulk elemental composition was quantified by inductively coupled plasma optical emission spectrometry (ICP-OES, Agilent) to determine the metal stoichiometry. Raman spectroscopy (model LabRAM HR Evolution, Horiba, Japan) was used to analyze the composition of samples after the reaction, with a 532 nm laser as the excitation source. An ion chromatograph (model ICS-5000+, Thermo Fisher Scientific, USA) was used to quantify the concentrations of NO_2^- and NO_3^- after 24 hours of the ammonia oxidation reaction (AOR). N_2 adsorption-desorption isotherms were measured on a Micromeritics ASAP 2460 surface area and porosity analyzer (USA) to evaluate the specific surface area and pore structure of the catalyst. In situ attenuated total reflectance surface-enhanced infrared absorption spectroscopy (ATR-SEIRAS) was conducted using a Fourier-transform infrared spectrometer (model Nicolet 6700, Thermo Fisher Scientific, USA) to investigate the AOR process. The spectral resolution was set to 8 cm^{-1}, and a 60° Si prism was used as the reflective element. The WCuNiMo catalyst was affixed to a gold film on the working electrode, with a platinum wire as the counter

electrode and Ag/AgCl as the reference electrode. All experiments were conducted in a mixed solution of KOH and ammonia. A UV-vis spectrophotometer (model Cary 5000, Agilent Technologies, USA) was used to measure absorbance spectra. The absorbance intensity of $NH_3 \cdot H_2O$ was monitored at 655 nm to assess its concentration. The ammonia removal rate was calculated using the following equation:

$$R_{NH3 \cdot H2O} = C_t - C_0 \setminus C0 \times 100\%$$

Where C_t is the ammonia concentration after electrolysis, and C_0 is the initial concentration.

Electrochemical Characterization of Materials

Electrochemical measurements were conducted at room temperature using a Gamry Instruments Interface 5000E electrochemical workstation. The configuration consisted of a Ni foam-supported WCuNiMo catalyst as the working electrode, a carbon rod as the counter electrode, and a Hg/HgO electrode as the reference electrode. The geometric area of the working electrode was fixed at 1 × 1 cm^2. AOR and OER were measured in 1.0 M KOH containing 0.5 M ammonia and in pure 1.0 M KOH, respectively. All potentials were converted to the reversible hydrogen electrode (RHE) scale using the equation:

$$E_{RHE} = E_{Hg/HgO} + 0.059 \times pH + 0.098\ V$$

All electrochemical potentials were referenced to the reversible hydrogen electrode (RHE) with 90% iR compensation applied to correct for ohmic potential drop. Cyclic voltammetry (CV) was conducted to activate the catalyst within a potential window of 0-0.8 V vs. Hg/HgO at a scan rate of 100 mV s^{-1}. Linear sweep voltammetry (LSV) was performed from 0-1 V vs. Hg/HgO at a scan rate of 10 mV s^{-1} to evaluate electrocatalytic activity. Tafel slopes were derived by plotting the logarithm of the absolute current density (log|j|) against the corresponding overpotentials, with linear fitting of the relevant region to assess reaction kinetics. Electrochemical impedance spectroscopy (EIS) was carried out at fixed potentials of 0.5 V (AOR) and -1.14 V (HER) vs. Hg/HgO, using a sinusoidal perturbation of 5 mV over a frequency range of 10^5-0.1 Hz to analyze charge-transfer resistance. The double-layer capacitance (C_{dl} and electrochemically active surface area (ECSA) were estimated via CV measurements in the non-faradaic region at scan rates ranging from 20-100 mV s^{-1}; C_{dl} was determined from the slope of the linear fit of scan rate versus the

average current density. Chronoamperometry (i-t) at a fixed potential of 1.37 V was employed to evaluate the long-term stability of the catalyst for AOR, while chronopotentiometry (V-t) at a current density of 10 mA cm^{-2} was used to assess HER stability. Two electrode measurements were conducted by LSV in the range of 1-2 V at a scan rate of 10 mV s^{-1}, using the self-supported catalyst as both anode and cathode under ambient conditions.

Simulated Industrial Alkaline Electrolyzer Assembly

A simulated industrial-scale alkaline flow-type electrolyzer system was constructed to evaluate the bifunctional performance of the WCuNiMo catalyst and assess its practical application potential. Both the anode and cathode were loaded with 1 × 1 cm^2 of the alloy catalyst. A commercial polyphenylene sulfide (PPS) membrane with high ionic conductivity, gas barrier properties, and hydrophilicity was used to separate the electrodes. The current collector and endplates were fabricated from 1 mm and 5 mm thick high-purity titanium plates, respectively, with uniform dimensions of 5 × 5 cm^2, forming a symmetric cell structure with excellent strength and corrosion resistance. The electrolyte consisted of a mixed solution of 1 M KOH and 0.5 M ammonia, which was circulated through the anode and cathode chambers at identical flow rates using a pump to enhance mass transfer and facilitate the electrolysis process.

Figure S1. Photographic images of the synthesized alloy electrocatalysts: (a) WCuNiMo, (b) WNiMo, and (c) CuNiMo.

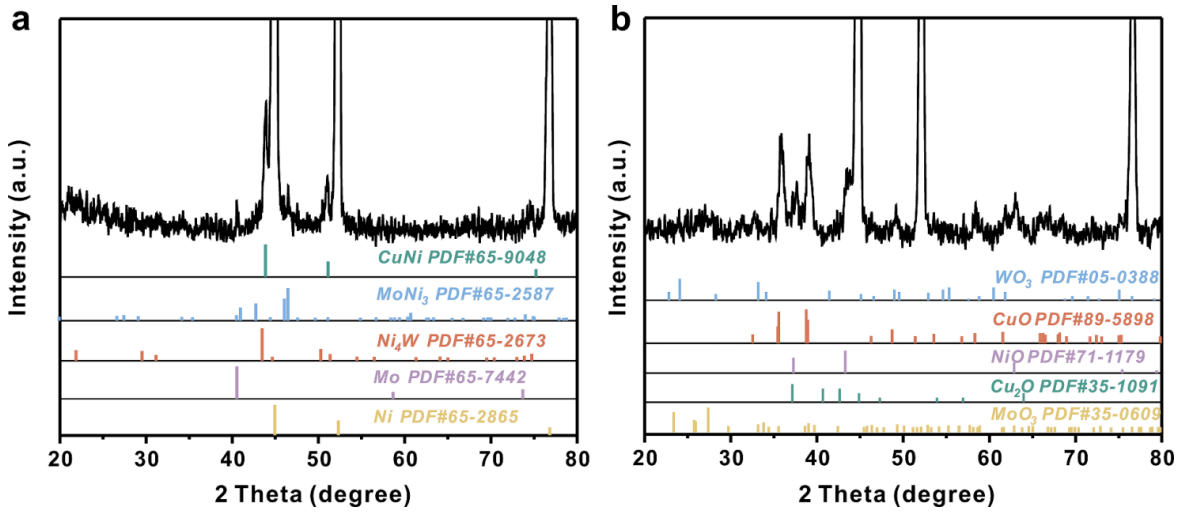

Figure S2. XRD patterns of the WCuNiMo alloy and WCuNiMoO_x multimetallic oxide catalysts: (a) WCuNiMo, (b) WCuNiMoO_x.

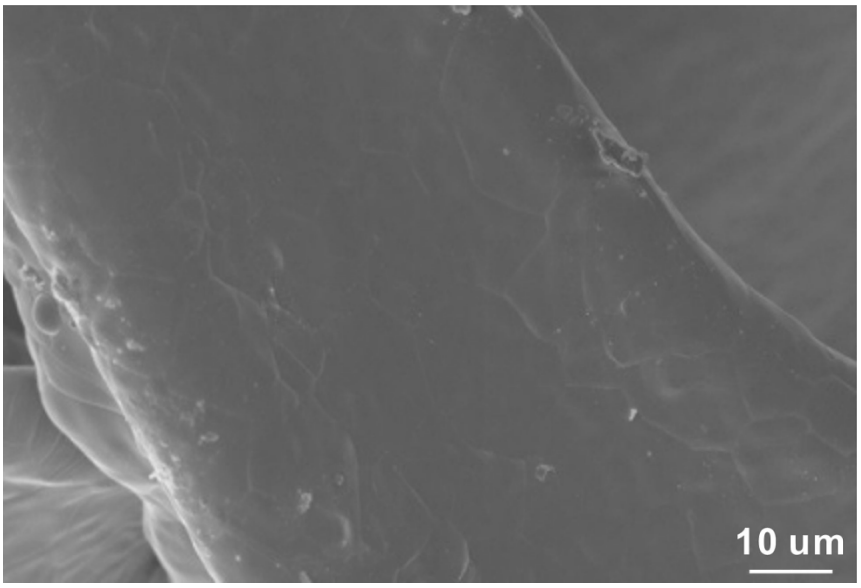

Figure S3. SEM image of pristine commercial Ni foam.

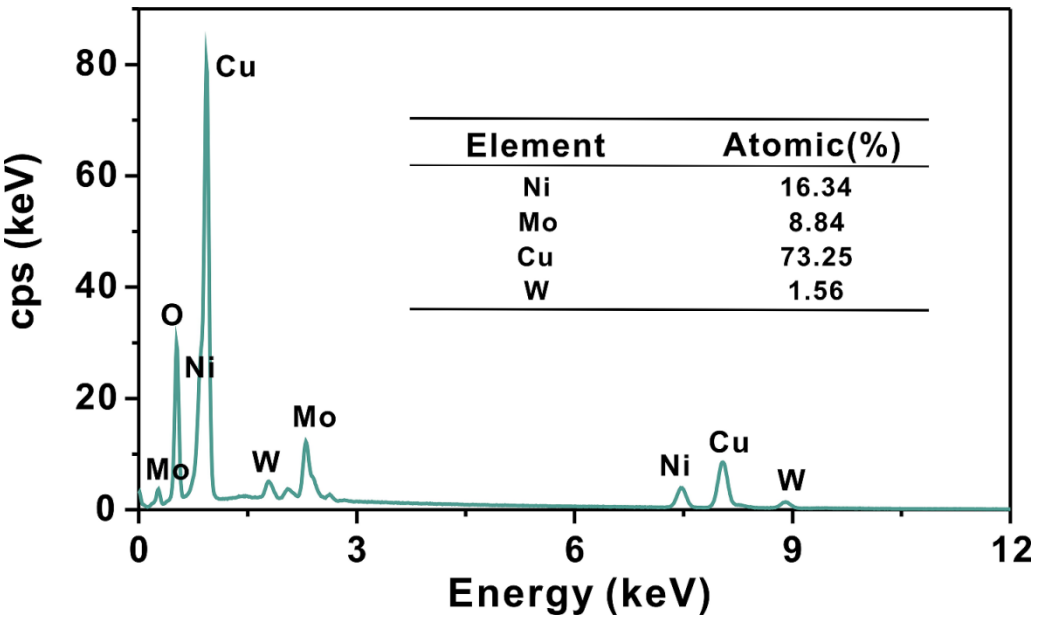

Figure S4. Quantitative EDS analysis of WCuNiMo alloy.

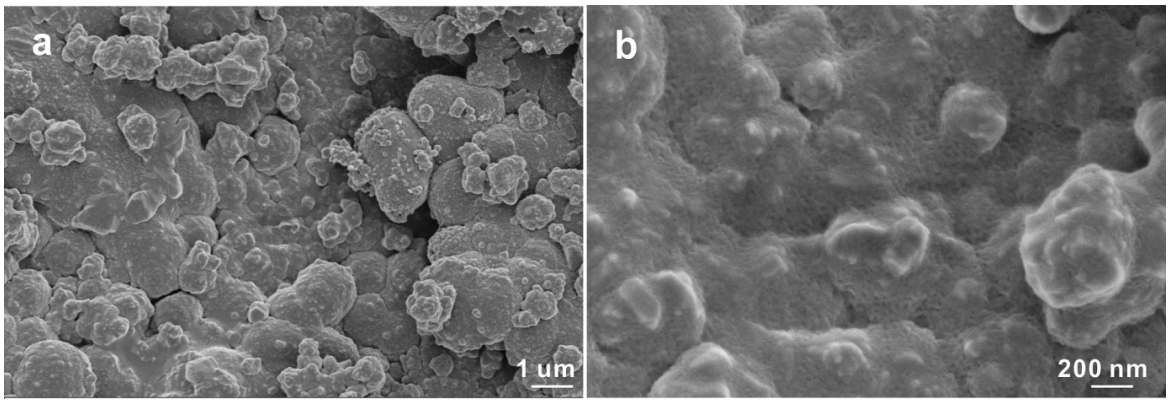

Figure S5. (a) Low- and (b) High-magnification SEM micrographs of $WCuNiMoO_x$ multimetallic oxide catalysts

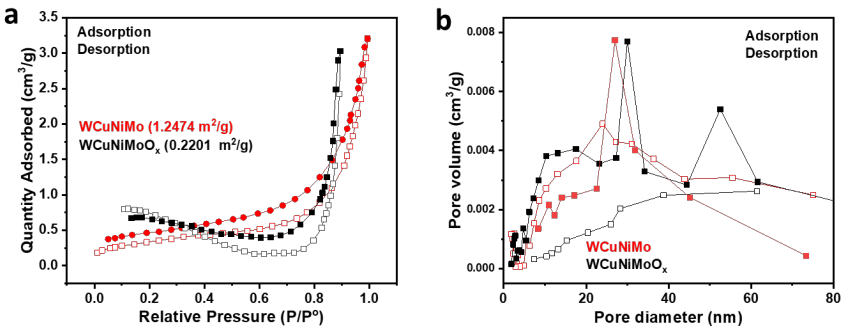

Figure S6. N_2 adsorption–desorption isotherms and corresponding BJH pore size distribution of the WCuNiMo and $WCuNiMoO_x$ catalysts.

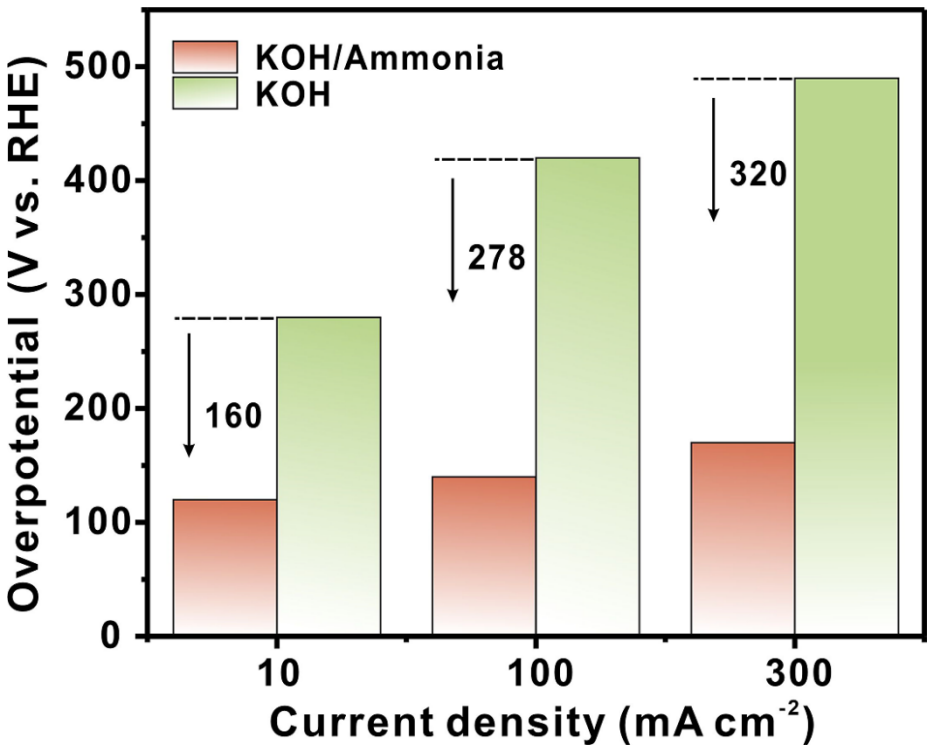

Figure S7. Comparison of overpotentials at 10, 100, and 300 mA·cm^{-2} for WCuNiMo alloy in KOH and KOH/NH_3 electrolytes.

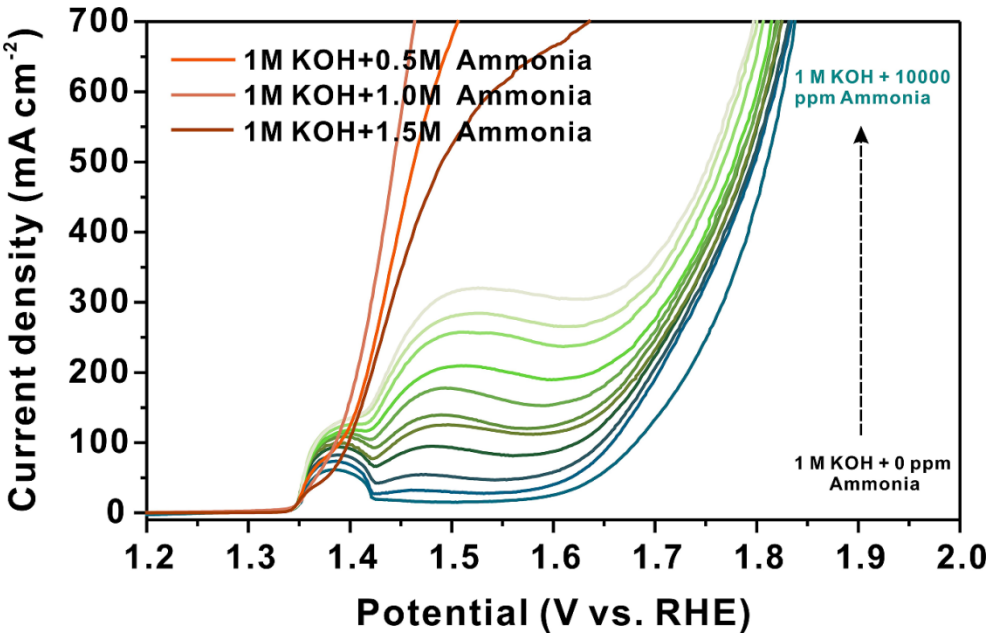

Figure S8. Polarization curves of WCuNiMo alloy catalyst in electrolytes with varying ammonia concentrations.

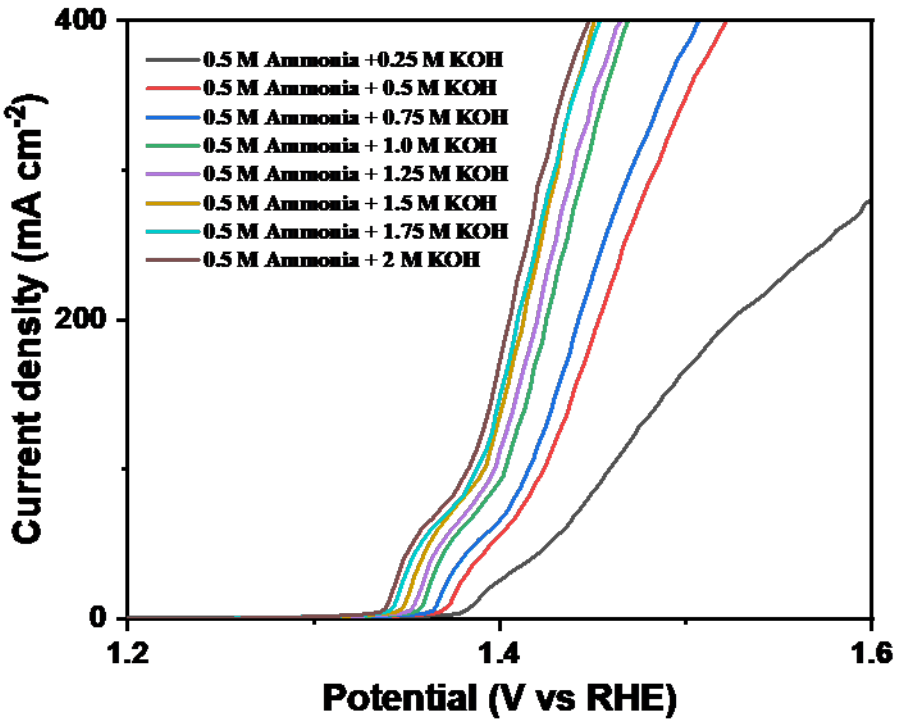

Figure S9. LSV curves of WCuNiMo in 0.5 M NH_3 with different KOH concentrations (0.25–2.0 M).

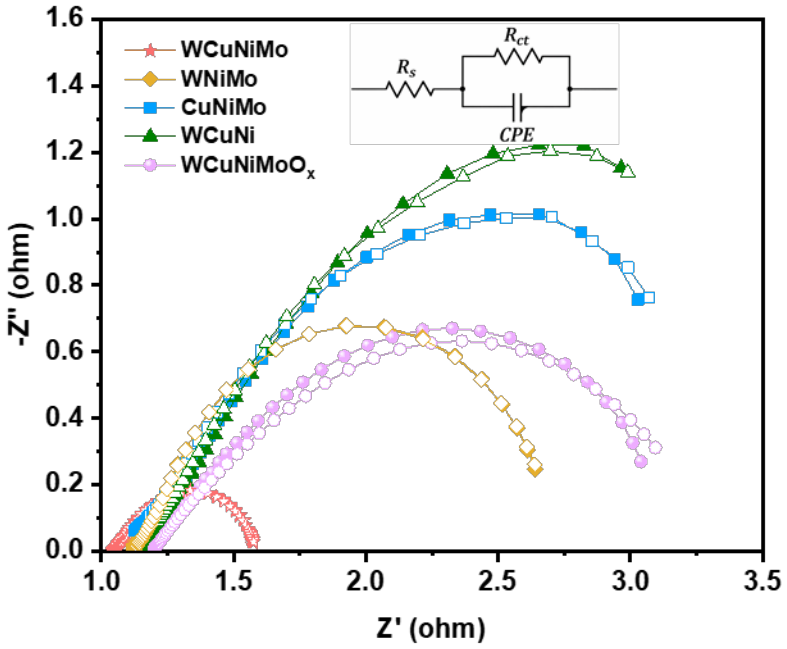

Figure S10. Nyquist plots and corresponding equivalent circuit used for fitting the EIS data.

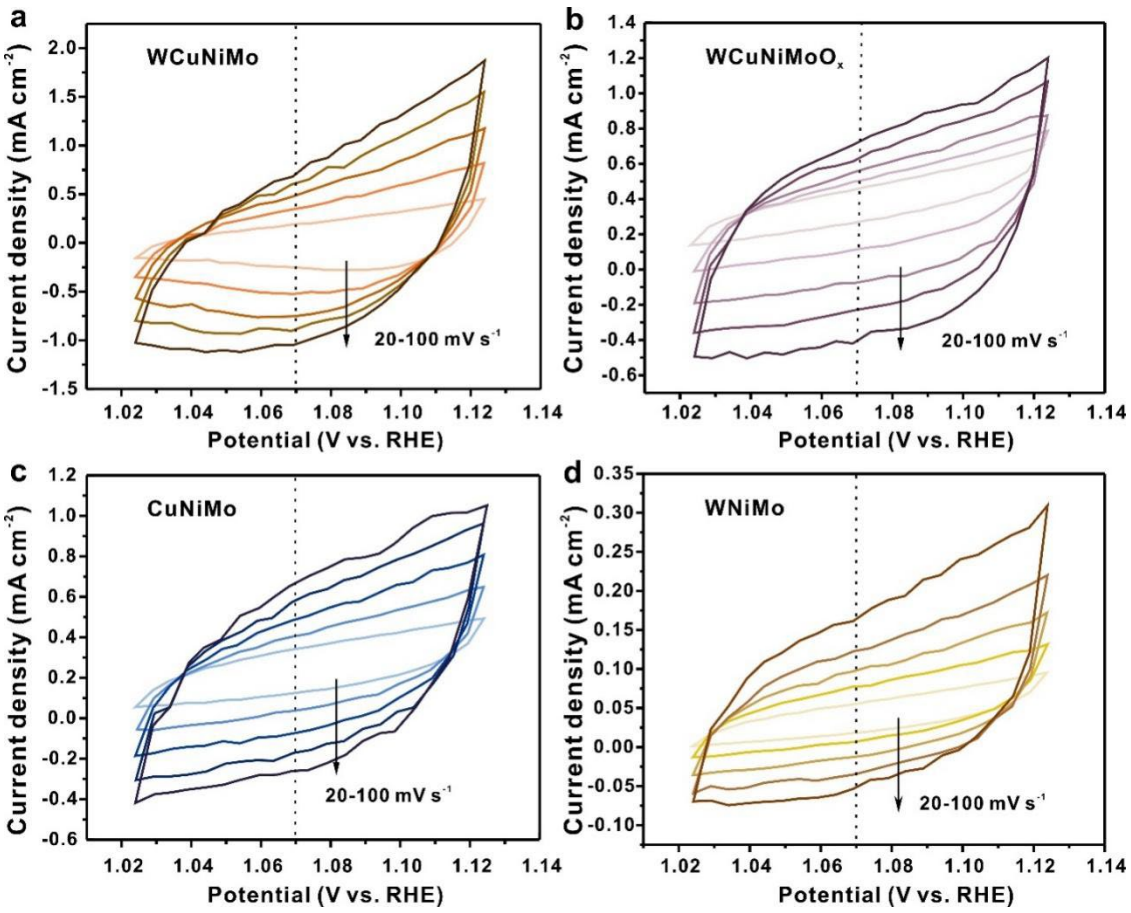

Figure S11. Cyclic voltammetry curves of synthesized catalysts in the non-Faradaic region at various scan rates.

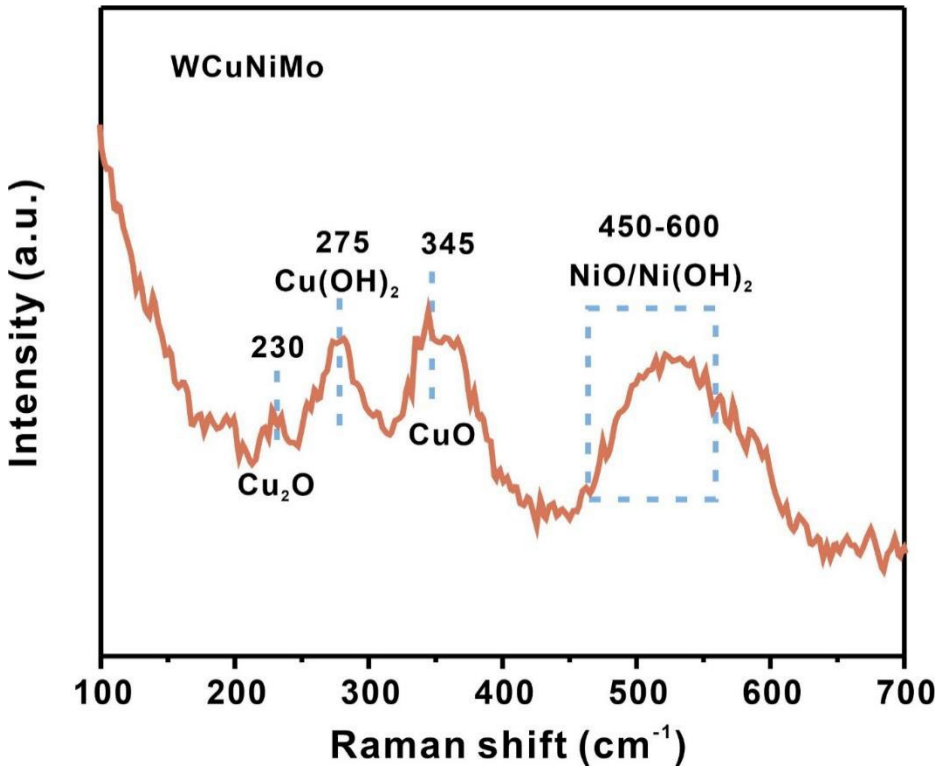

Figure S12. Raman spectrum of the WCuNiMo catalyst after AOR

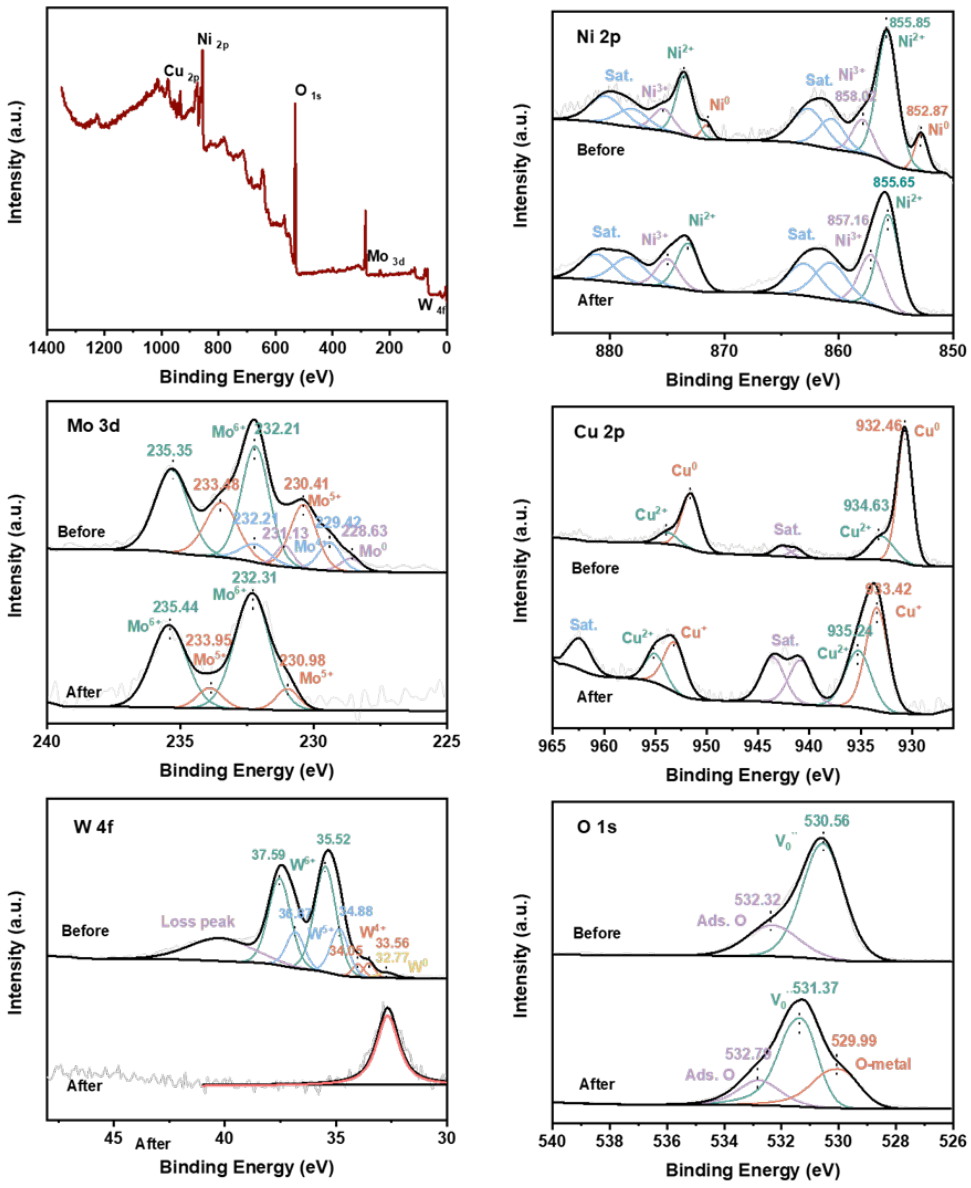

Figure S13. XPS spectra of WCuNiMo before and after stability testing

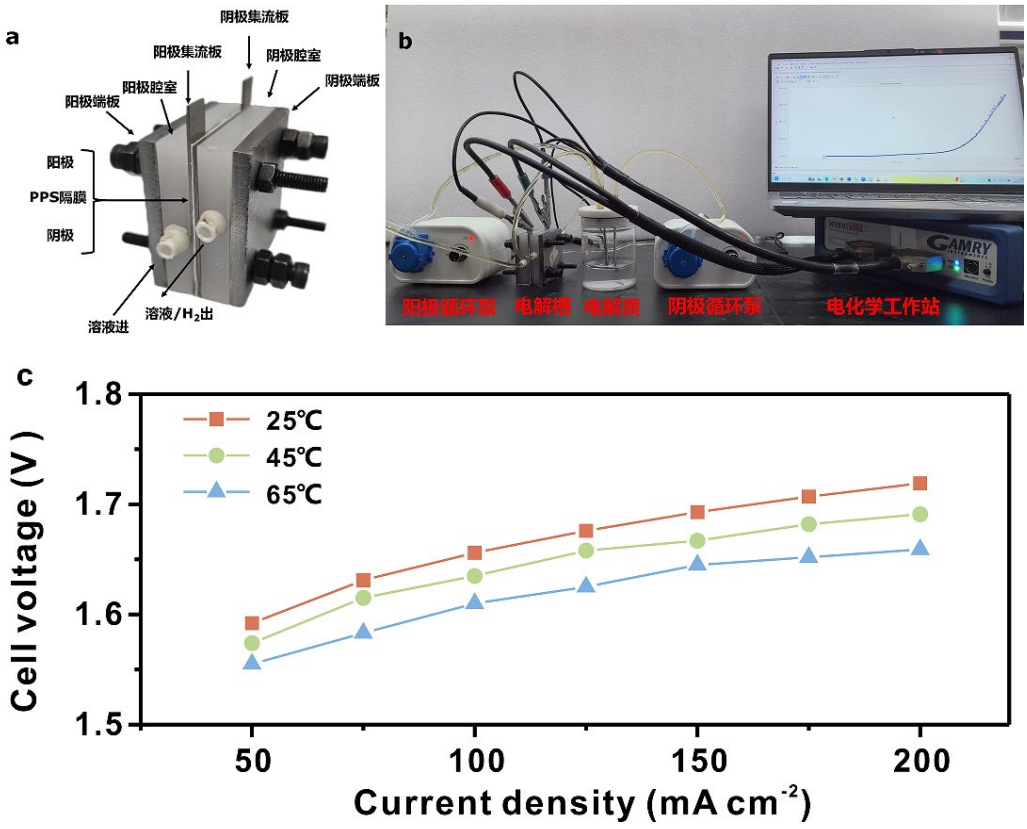

Figure S14. (a) Schematic diagram of the electrolyzer components used in this study, (b) Simulated test of the electrolyzer, (c) Electrolyzer performance at different operating temperatures.

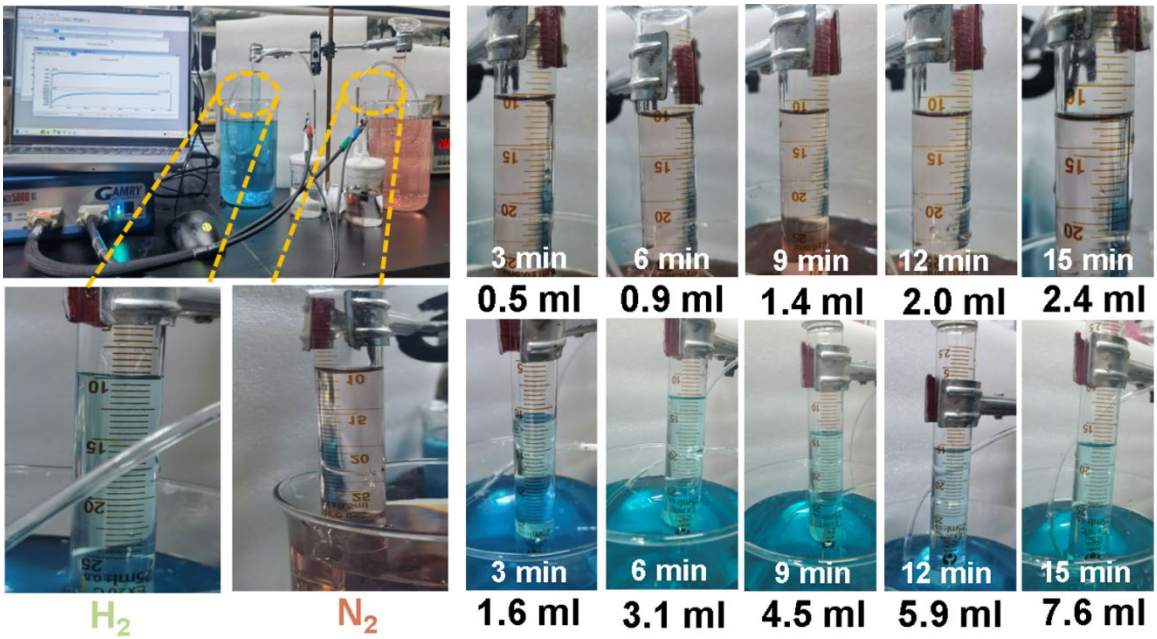

Figure S15. Schematic of the H-type electrolyzer setup for gas production monitoring using WCuNiMo catalyst.

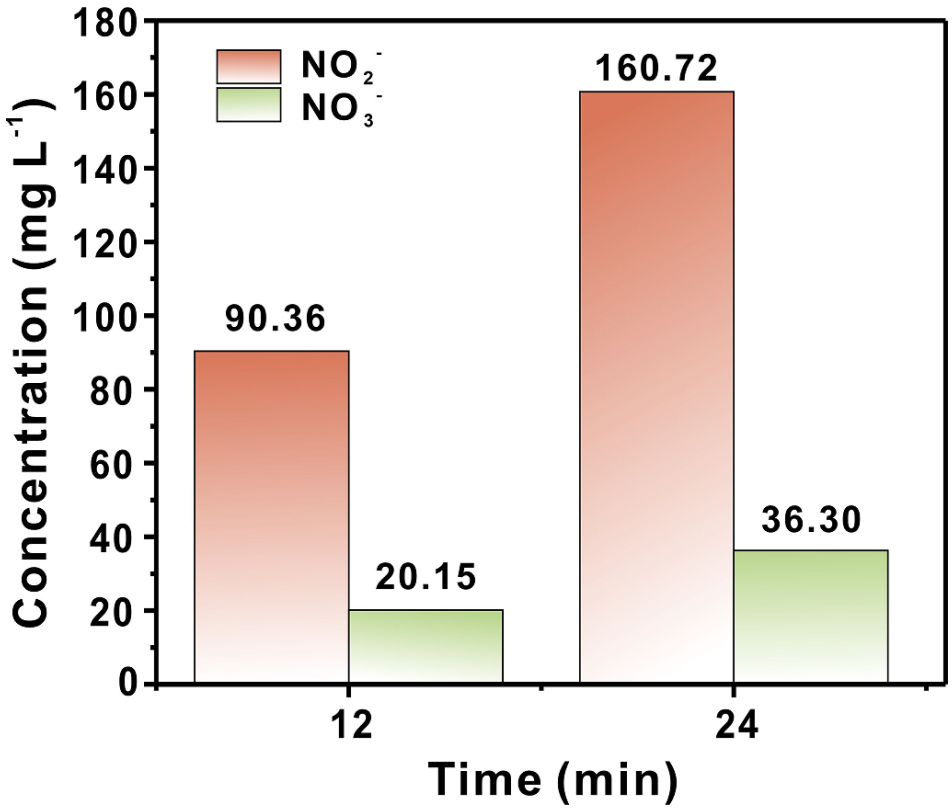

Figure S16. Ion chromatography analysis of NO_2^- and NO_3^- generation after 12 and 24 hours of electrolysis using WCuNiMo catalyst

Table S1. ICP-OES analysis of the elemental composition of the WCuNiMo catalyst, showing the weight percentages of W, Mo, Cu, and Ni

S/No.	Elements	Wt.%
1	W	0.86
2	Mo	0.09
3	Cu	4.32
4	Ni	94.44

Table S2. Comparison performance of PGM-based AOR electrocatalysts.

Catalyst	Electrolyte	Peak Potential	Peak current density ($mA\ cm^{-2}$)	Reference
Pt–M nanocube (M = (Fe, Co, Ni, Zn))	0.1 M KOH + 0.1 M NH3	≈ 0.7 V	1.685 mA cm^{-2}	[1]
Pt NPs	1 M NH3 + 1 M KOH	−0.13 V	≈58 mA cm^{-2}	[2]
Pt/Ir/MWCNT NPs	0.1 M NH3 + 0.1 M KOH	≈ 0.74 V	≈0.23 mA cm^{-2}	[3]
Pt NPs Nickel oxide carrier	1 M KOH + 0.2 M NH4OH	−0.23 V	≈0.93 mA cm^{-2}	[4]
IrRh/C	1 M KOH + 2 M NH4OH	≈− 0.32 V	Not reported	[5]
Au@Pt NPs	0.5 M NaOH + 0.055 M NH4Cl	≈0.68 V	Not reported	[6]
Pt NPs	1 M KOH + 0.1 M NH3	≈−0.36 V	Not reported	[7]
WCuNiMo	1M KOH +0.5 M NH_3	0.79 V	49.03 mA cm^{-2}	This work

Table S3. Comparison performance of non PGM-based AOR electrocatalysts.

Catalyst	Electrolyte	Onset potential	Current density (mA cm^{-2})	Reference
NiCu/CP	0.5 M NaOH + 55 mM NH_4Cl	0.47 V vs. Ag/AgCl	52 @0.70 V vs. Ag/AgCl	[8]
NiCuC	0.5 M KOH + 0.5 M NH_3	0.47 V vs. Hg/HgO	38.2 @0.70 V vs. Hg/HgO	[9]
Ni-Cu-Co/CNT	1 M KOH + 0.5 M NH_3	0.3 V vs. Ag/AgCl	96 @0.80 V vs. Ag/AgCl	[10]
$Ni1Cu_3$@Ni-NDC	1 M KOH + 0.5 M NH_3	1.3 V vs. RHE	120 @1.90 V vs. RHE	[11]
NiCu/BDD	0.5 M NaOH + 0.5 M NH_3-N	0.345 V vs. Ag/AgCl	38.94 @0.54 V vs. Ag/AgCl	[12]
$NiSe_2$/Se-NiCuOx/NF	1 M NaOH + 0.5 M NH_4Cl	1.16 V vs. RHE	225 @1.80 V vs. RHE	[13]
NiCu/MnO_2	0.5 M KOH + 55 mM NH_4Cl	0.45 V vs. Hg/HgO	31 @0.80 V vs. Hg/HgO	[14]
a-NiCuFe	0.5 M NaOH + 55 mM NH_4Cl	0.35 V vs. SCE	60 @0.70 V vs. SCE	[15]
NiCu DHTs	0.05 M NH4OH + 0.1 M NaOH	1.31 V vs. RHE	7.52 @1.50 V vs. RHE	[16]
$Ni_{0.8}Cu_{0.2}$ LHs	0.5 M NaOH + 55 mM NH_4Cl	0.43 V vs. Ag/AgCl	35 @0.55 V vs. Ag/AgCl	[17]
Ag/Ni	1.5 M NaOH + 0.5 M NH3	0.46 V vs. Hg/HgO	46.7 @0.70 V vs. Hg/HgO	[18]
Cu8Ni2	0.5 M KOH + 55 mM NH4Cl	1.4 V vs. RHE	53 @1.70 V vs. RHE	[19]
WCuNiMo	1.0 M KOH + 0.5 M NH_3	1.34 V vs. RHE	100 @ 1.37 V vs. RHE	This work

References

1. Y. T. Chan, K. Siddharth and M. Shao, *Nano Res.* 2020, **13**, 1920-1927.
2. N. Hanada, Y. Kohase, K. Hori, H. Sugime and S. Noda, *Electrochim. Acta,* 2020, **341**, 136027.
3. S. Morita, E. Kudo, R. Shirasaka, M. Yonekawa, K. Nagai, H. Ota, M. N.-. Gamo and H. Shiroishi, *J. Electroanal. Chem.* 2016, **762**, 29-36.
4. S. Ntais, A. Serov, N. I. Andersen, A. J. Roy, E. Cossar, A. Allagui, Z. Lu, X. Cui, E. A. Baranova and P. Atanassov, *Electrochimic Acta*, 2016, **222**, 1455-1463.
5. R. A. Martínez-Rodríguez, F. J. Vidal-Iglesias, J. Solla-Gullón, C. R. Cabrera and J. M. Feliu, *ChemElectroChem*, 2016, **3**, 1601-1608.
6. J. Wang, J. Heo, C. Chen, A. J. Wilson and P. K. Jain, *Angew. Chem.* 2020, **132**, 18588-18592.
7. J. Liu, X. Du, Y. Yang, Y. Deng, W. Hu and C. Zhong, *Electrochem. Commun.* 2015, **58**, 6-10.
8. W. Xu, D. Du, R. Lan, J. Humphreys, D. N. Miller, M. Walker, Z. Wu, J. T. Irvine and S. Tao, *Appl. Catal. B Environ.* 2018, **237**, 1101-1109.
9. U. Kim, J. Choi and S. Lee, *Int. J. Hydrogen Energy* 2025, **105**, 126-136.
10. Z. Liu, M. Wu and J. Ma, *Energy & Fuels*, 2022, **36**, 10339-10345.
11. J. Chen, H. Chen, Z. Wang, Y. Fu, D. Yu, J. Liang, Y. Huang, L. Wang, I. T. Bello and G. N. Ekambo, *Chem. Eng. J.* 2024, **499**, 156283.
12. J. Song, Y. Yinhai, Y. Jia, T. Wang, J. Wei, M. Wang, S. Zhou, Z. Li, Y. Hou and L. Lei, *Sep. Purif. Technol.* 2021, **276**, 119350.
13. G.-L. Li, T.-G. Ma, Y.-H. Shi, F. Deng, R.-Y. Huang, Y. Yan, Q. Mao, Y. Li and Y. Xiao, *Chem. Eng. J.* 2024, **502**, 158096.
14. K. Nagita, Y. Yuhara, K. Fujii, Y. Katayama and M. Nakayama, *ACS Appl. Mater. Interfaces* 2021, **13**, 28098-28107.
15. M. Zhu, Y. Yang, S. Xi, C. Diao, Z. Yu, W. S. V. Lee and J. Xue, *Small*, 2021, **17**, 2005616.
16. A. Yang, J. Wang, K. Su, W. Lei, X. Qiu and Y. Tang, *Chem. Eur. J.* 2021, **27**, 4869-4875.
17. W. Xu, R. Lan, D. Du, J. Humphreys, M. Walker, Z. Wu, H. Wang and S. Tao, *Appl. Catal. B Environ.* 2017, **218**, 470-479.
18. Y. Jin, X. Chen and J. Wang, *Chem. Commun.* 2022, **58**, 10631-10634.
19. Z. Mao, Y. Tian, B. Guo, R. Chen, Y. Zeng, F. Hou, X. Yan and J. Liang, *Chem. Eng. J.* 2024, **484**, 149570.